Advanced seismological analysis of a complex seismic event at LaRonde mine

Stephen Meyer [a,*], Christopher Durham [b], Véronique Falmagne [c]

[a] *Institute of Mine Seismology, Canada*

[b] *LaRonde mine, Agnico Eagle Mines, Canada*

[c] *Agnico Eagle Mines, Canada*

Abstract

The LaRonde mine has been in continuous operation since 1988, with mining undertaken from near surface to a current depth of 3,260 m, and reserves and resources extending deeper. Over the past decade mining-induced seismicity at great depths has become a significant challenge at LaRonde. Strategic and tactical control measures have been successfully implemented to manage seismic risks and promote a safe working environment. As mining progresses ever deeper, the enhanced analysis of seismic data can support a more comprehensive understanding of the increased dynamic responses of rock masses and structural behaviours subject to varying stresses and deformations induced by mining. This advanced understanding is needed to continue to improve the mine design, optimise ground support schemes and plan the ore extraction sequence, thereby contributing to the management of seismic risk.

In August 2023 the mine experienced a significant seismic event around the 317–320 levels of the East mine. Bulking and excavation damage were observed in multiple locations, some away from the initially processed event location. An advanced seismic analysis was undertaken to help understand and explain the processes and observations associated with the event. Seismic data from a regional network on the surface was combined with that from the in-mine system to improve seismic source parameter estimates. The recorded waveforms contain multiple phases, indicating a complex event driven by more than a single failure mechanism occurring over an extended volume. A finite source inversion was undertaken to provide a more realistic description of the source process, how it is distributed in space and how it evolved in time. The findings illustrate that large seismic events in mines need to be considered as regions of deformation where the failure mechanisms can vary and that traditional approaches, such as a point source approximation and peak ground velocity-focused analyses, are inadequate for such scenarios.

Keywords: *seismicity, rockburst, moment tensor, finite source inversion, mining-induced seismicity*

1   Introduction

The LaRonde mine produces base and precious metals from a world-class volcanogenic massive sulfide (VMS) deposit composed of ore lenses rich in gold (Au), with silver (Ag), copper (Cu) and zinc (Zn). This Agnico Eagle property is located between Rouyn-Noranda and Val-d'Or, in the Abitibi-Témiscamingue region of northwestern Quebec, Canada. The LaRonde deposit, located in the Neoarchean southern Abitibi greenstone belt (Monecke et al. 2017), comprises east–west striking Au-Ag-Cu-Zn lenses which dip at about 75 to 80° south with a westerly plunge.

The LaRonde mine has been in continuous operation since 1988, initially starting from near the surface and currently extending to a depth of 3,260 m, with reserves/resources extending even deeper. With a daily production rate of 4,200 tonnes hoisted, LaRonde is recognised as one of the deepest and most highly

---

[*] Corresponding author. Email address: stephen.meyer@imsi.org

stressed mines in Canada and in the world. Mining operations at LaRonde utilise a transverse open stoping method with delayed backfill. This approach involves both overhand and underhand sequences, incorporating primary-secondary and pillarless sequences. Operations below level 269 (2,690 m below surface) are divided into two main sectors: East and West mines (Figure 1).
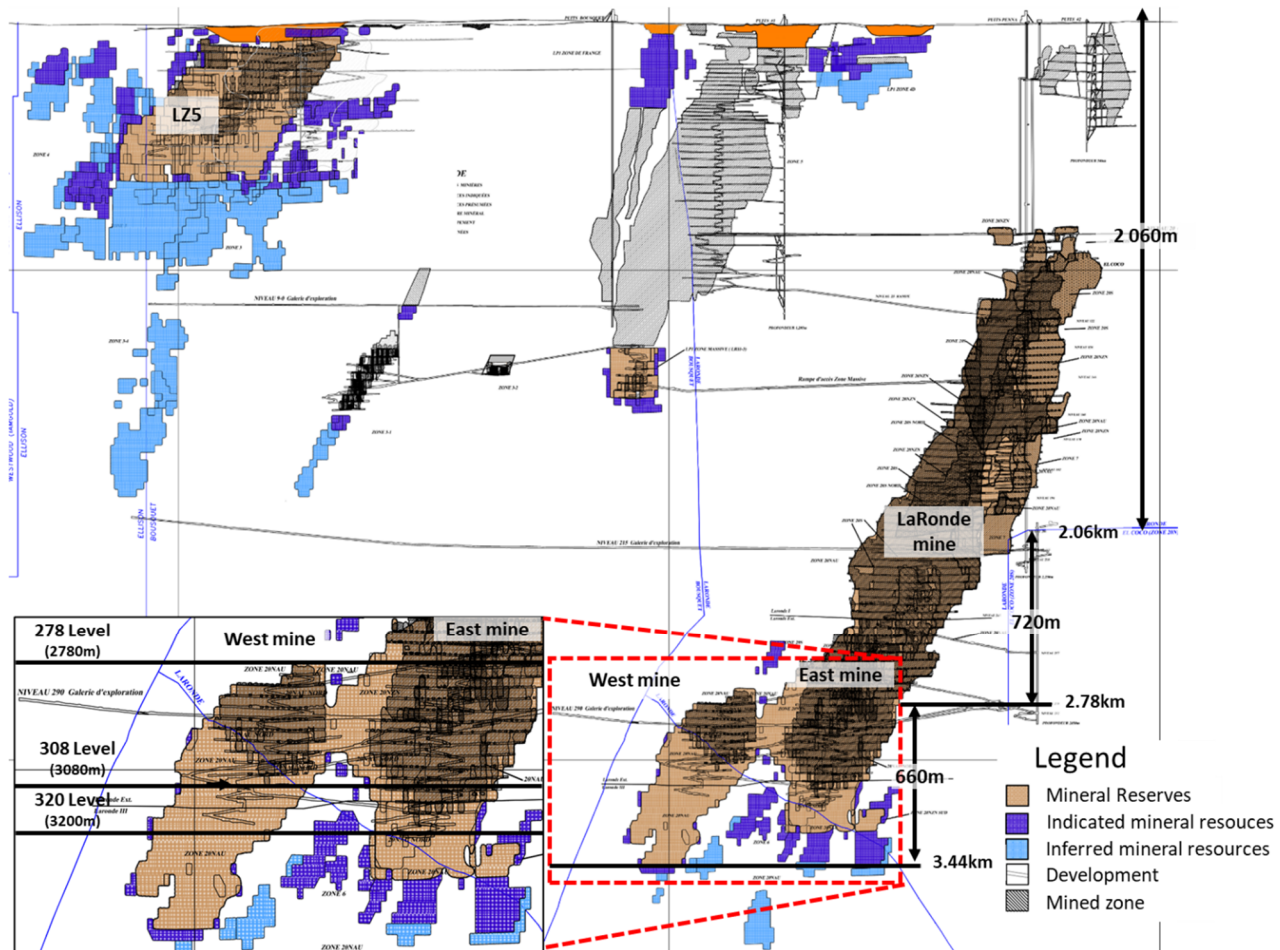

Figure 1   Longitudinal view of the LaRonde complex mineral reserves and infrastructure, 2024

Over the past decade, ground control challenges at the LaRonde mine have been primarily associated with managing mining-induced seismicity associated with high-stress conditions at great depths. Strategic and tactical control measures have been successfully implemented to mitigate seismicity and foster a safe working environment, as described by Sasseville et al. (2022). As mining progresses to ever-greater depths, the enhancement of seismic data analysis can contribute to the understanding of the dynamic responses of rock masses and their structural behaviours under varying stresses and deformations induced by mining activities.

The East and West mine zones host most of the current mine development, predominantly in the footwall of the orebody which lies to its north. The footwall is composed of two principal rock units. The first is rhyolite/rhyodacite tuff (V9i and V9a [altered]). This unit contains sheared and altered corridors in the immediate ore footwall, where the main drawpoints and development drifts are located. The second is basalt-andesite (V6 and V7). These rock types are found further north of the orebody and also host some of the permanent mine infrastructure.

The geomechanical behaviour of the rock mass is significantly influenced by a strong regional schistosity parallel to the orebody. The rhyolite/rhyodacite unit (V9i-V9a) is characterised by east–west striking foliation with a steep dip angle of 80°. The foliation spacing ranges between 0.016 and 0.076 m, with tighter spacing observed nearer to the orebody (Karampinos et al. 2015). This unit is distinguished by shear corridors along the schistosity that present varying levels of sericite alteration and silicification. The combined effects of

shearing and alteration lead to significant variations in the unit's composition and texture, and anisotropy in geomechanical properties, such as stiffness and shear strength. The mining-induced stress redistribution within the footwall results in deformation contrasts across these shear corridors, making them typical sources of seismic activity at LaRonde.

Seismicity rates increase at deeper mine levels where the rock mass not only experiences higher stress conditions but also exhibits increased stiffness and strength, as evidenced by the increase in uniaxial compressive strength (UCS), and Young's modulus (E) (Goulet et al. 2018a, 2018b). The results of the intact rock strength testing for each geomechanical domain below level 281 are detailed in Table 1 (Ouellet et al. 2024). At the bottom of the mine where the production and development activities are located, the in situ stress levels surpass 100 MPa, based on the results of stress measurements at the mine presented in Table 2, which were evaluated using the 'doorstopper' approach coupled with an acoustic televiewer borehole logging approach (Corthésy 2006; DGI Geoscience Inc. 2017).

Table 1   Hoek–Brown (Hoek 1994) strength parameters for intact rock, per domain

Geomechanical domain	Number of specimens	σ_{ci}(UCS) (MPa)	m_i	Coefficient of determination (R²)
V6 – andesite	5	200	14.9	0.42
V7 – basalt	9	249	17	0.61
V9i – ryholite tuff	22	201	12.2	0.44
V9a – altered V9i	19	199	15.9	0.76
Ore – volcanogenic massive sulphide	5	183	12.2	0.68

Table 2   Major principal stresses at the LaRonde mine

Major principal stress	Orientation (trend, plunge)	Equation
σ₃ = σᵥ	125°, 71°	0.027 MPa/m (depth)
σ₁	010°, 09°	1.62σᵥ
σ₂	277°, 17°	1.34σᵥ

With a daily seismic rate of about 2,000 events recorded in 2023, the underground seismic system at LaRonde mine is designed to deliver high location accuracy and reliable source parameters. The current underground monitoring system comprises 107 uniaxial accelerometers (50 Hz), 26 triaxial accelerometers (50 Hz) and 39 geophones (15 Hz), effectively capturing events ranging from moment magnitude (MW) (Hanks & Kanamori 1979) –3 to 2. However, during large seismic events (greater than MW2), the underground seismic system can become saturated, leading to accurate event locations but misrepresented source parameters due to its limited dynamic range (see Boore 1986 for a detailed description of the issue). To address this limitation, a regional seismic system composed of 13 surface geophones (4.5 Hz) installed in nearby communities is used to supplement the data and provide more accurate source parameters for large events.

On 29 August 2023 LaRonde mine experienced a significant seismic event (MW2.5) around the 317–320 levels of the East mine. This event led to bulking and excavation damage at multiple locations, some of which were distant from the initially processed event location. The complexity of this seismic event was highlighted by the recorded waveforms, which contained multiple phases. This suggested that the seismic activity was driven by more than a single failure mechanism and occurred over an extended volume. To better understand the failure processes and the observed damage associated with this event, advanced seismic analyses were

conducted. This paper presents a detailed seismic analysis of this complex event and outlines the key findings from a seismological perspective.

2 Data preparation

Advanced analysis of a seismic event from a rock mechanics or geotechnical perspective requires two fundamental features of the seismic data to be addressed: the ability to locate the source of the event to reasonable accuracy, and to have verified sensor orientations to record the directions and polarities of the P-waves and S-waves allowing seismic source mechanism inversion. The ability to record accurate and reliable source parameters is also important, but this is more relevant when addressing seismicity as a whole and for medium- to long-term hazard assessments, and does not provide significant insight into the geotechnical details of a specific event. In this section we briefly cover the calibration of the velocity model and verification of sensor orientations that were required to facilitate the advanced analysis of the event.

An adaptive apparent velocities model (Nordström et al. 2017) was calibrated using a collection of seven blasts (both development and production), as shown in Figure 2. A larger set was provided but many of the blasts were unsuitable for use in the velocity model due to difficulties in accurate identification of sufficient P- and S-wave arrival times. Although more blasts may have been preferred, this study focuses on a single event for which these blasts provided reasonable coverage and were therefore considered appropriate. This number of blasts would be considered insufficient for a mine-wide velocity model, particularly for a mine of this size. An additional seven blasts were provided at a later stage, when most of the analysis had already been conducted. These were used as verification blasts, with the difference between the true and calculated location ranging from 5 to 25 m, and a median error of 13 m. The mainshock in question (and aftershocks) were relocated after updating the velocity model with the verification blasts. The resultant changes in location were small, only a few metres, and did not change the interpretation of any of the events. Significant variation in the apparent seismic velocities was observed, as shown in Figure 3. This indicates a complex velocity structure due to the geology, which contains significant structures and anisotropy, as well as the presence of a yielding zone around the existing production areas. It can be observed that none of the ray paths between the blast and sensors goes through (or around) stopes.
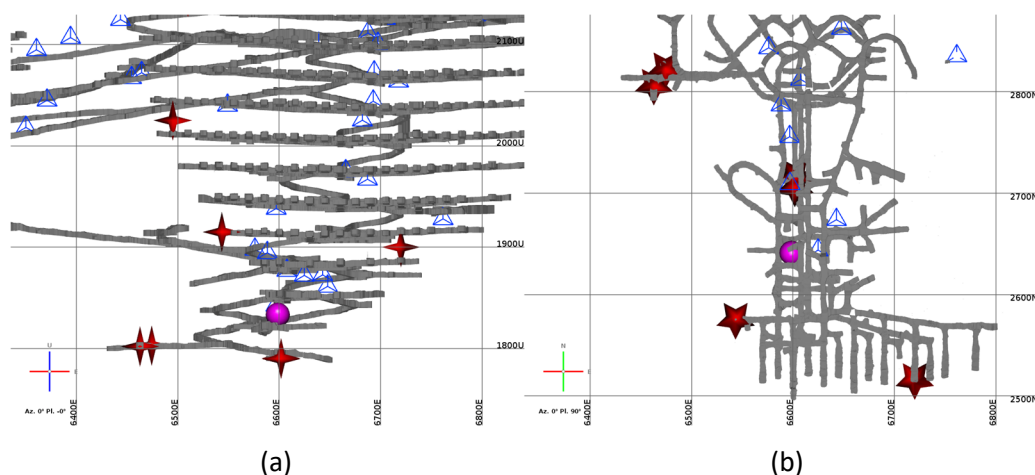

(a)   (b)

Figure 2 **(a) Section view looking north and (b) plan view clipped below Z = 1925 of the estimated event initiation location (purple sphere), calibration blasts (red stars) and operational sensors that provided at least some useful information in analysing the main event**

As the area of interest and seismic array are in the footwall, having stopes in direct line-of-sight of the source was not a significant source of error or uncertainty. Of the 35 triaxial geophones in the underground network, reliable sensor orientations could be inverted for 26 of them. The accelerometers (both uniaxial and triaxial)

are not appropriate for source mechanism inversion of large events due to their poor performance at low frequencies and susceptibility to clipping.
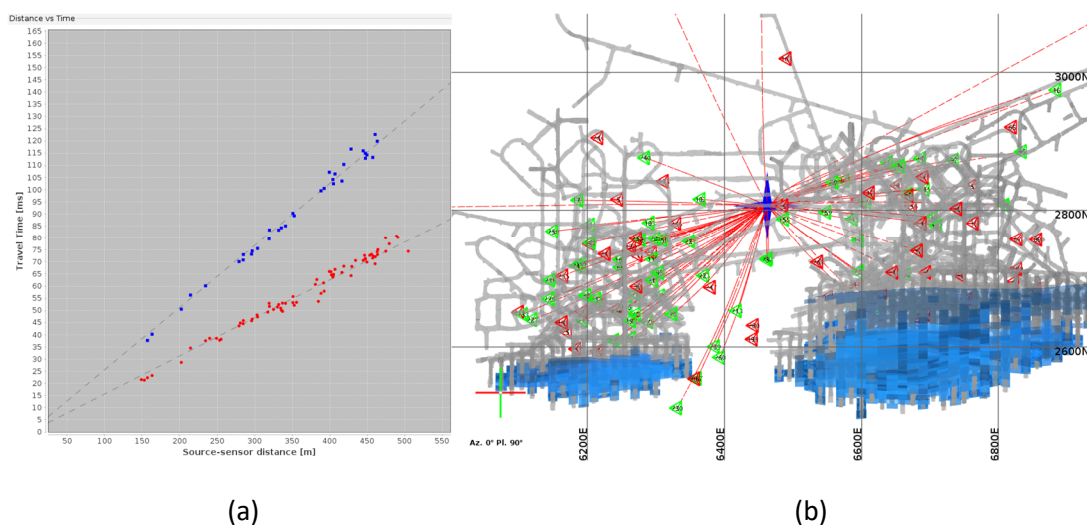

(a)   (b)

Figure 3   **(a) Travel time plot and (b) plan view of one of the blasts used in the adaptive apparent velocities model. Mined out stopes are shown in blue. Green symbols indicate operational sensors that could be used**

3   Analysis of the waveforms of the main event: standard processing

The waveforms generated by the event were complex, having long duration and containing multiple pairs of P-wave and S-wave arrivals, as illustrated in Figure 4. The initial P- and S-waves (P1, S1) are clear and easy to pick. Later, stronger arrivals are evident (S2, S3), however, accurately finding the corresponding P-pairs and S-pairs is difficult. The authors consider the overall event as a complex source which can be considered as a combination of subsources, each radiating its own P-waves and S-waves and having its own location, source mechanism and origin time. The waveforms were carefully inspected for mechanical clipping and digitiser saturation, which was present on a number of sensors, but not on the one shown in Figure 4.
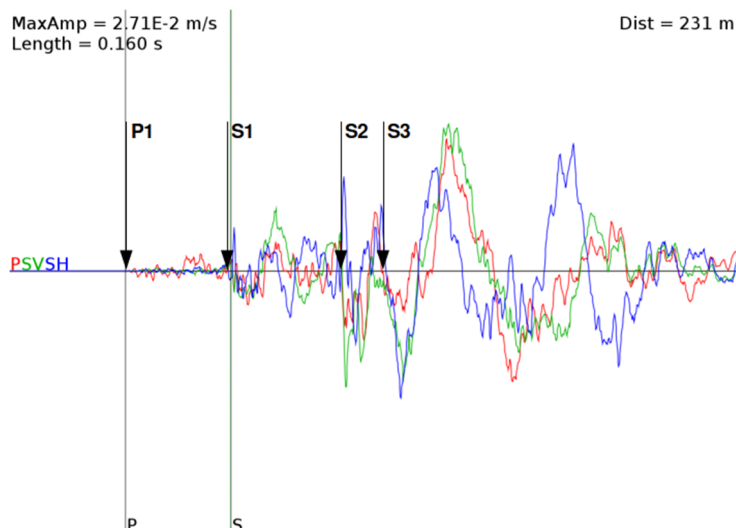

Figure 4   **Waveform of the main event recorded at one of the triaxial geophones, displayed in P-SV-SH (red-green-blue) components. S-wave arrivals 1 and 2 have the same polarity S-waves (SV down, SH up) and are characterised by sharp, impulsive arrivals. Arrival S3 shows a different polarity S-wave (SV and SH down), and with larger amplitude and lower frequency. Only P1 is shown as P2 and P3 are not clear**

The presence of these complex seismic waves with multiple phases indicates that the source was distributed in space (and time), and cannot be accurately represented by a simple point source approximation. This concept is illustrated in Figure 5. This can explain scenarios where damage is observed at multiple locations, often far from the processed seismic event location. The subsources are marked 1, 2, 3 and could hypothetically generate the respective P-wave and S-wave arrivals 1, 2, and 3 in Figure 4. The major source of damage located at excavation B may be due to subsource 3, which is located far from the processed event location 1.
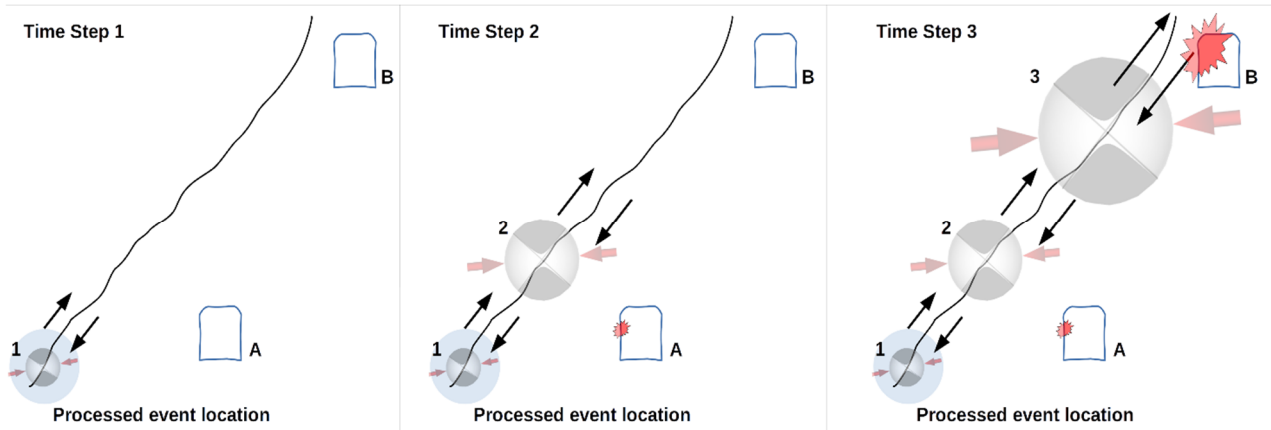

Figure 5   Illustration of a distributed fault slip seismic source. The event may initiate as a small, simple source (time step 1). The rupture may propagate further and increase deformation, and may lead to damage at another location (excavation A, time step 2) and later to more significant damage at an even-more remote location (excavation B, time step 3)

The initial P-wave and S-wave arrivals (P1, Figure 4) could be identified and picked with quite high accuracy, while the later arrivals were far less clear. However, estimating the location and location uncertainty of the later arrivals using traditional P- and S-wave picking may be possible. The location uncertainty region is then estimated for each pair of seismic wave arrivals using a Monte Carlo approach, varying the arrival times and apparent velocities within the uncertainty bounds. The arrival time uncertainty was based on the signal-to-noise ratio and frequency content of the waves. It varied from sensor to sensor, but was generally in the order of 1–4 ms for the first arrivals (Pair 1) and 7–10 ms for the later arrivals (Pair 3), due to the complex nature of the waveforms (shown in Figure 4). The uncertainty in the velocities was assumed to be up to 5% for both P-waves and S-waves. Figure 6 compares the estimated location uncertainty regions for the subsources associated with wave Pairs 1 (blue) and 3 (green). For each arrival the picks are identified as accurately as possible. The figure shows that the estimated source uncertainty region for the later phase is much larger, as expected, but also about 50 m to the south of the location of the initial phase, with no overlap between the uncertainty regions.

After estimating the location of the source, in this case subsource 1, which the authors consider the most accurately located, the following step was to determine the source parameters (magnitude, potency, energy) of the event, which was recorded as MN2.8 (Nuttli magnitude) by the national earthquake monitoring network (Government of Canada 2024). Due to the size of the event, the in-mine sensors are not expected to be able to achieve this accurately, for two reasons. Firstly, the sensors in the mine are high frequency accelerometers and 15 Hz geophones which would not be able to reliably capture the low frequencies associated with an event of this magnitude. Secondly, even if the in-mine sensors could capture the lower frequencies, they are likely situated too close to the source. Proper estimation of seismic source parameters requires that the sensors are situated far enough away from the source so that they can be considered in the far field (Gibowicz & Kijko 1994). This usually implies on the order of a few times the wavelength of the waves of interest, although there is no strict definition, but more than two at least. For example, considering Figure 7, if one assumes a strain change of 10^{-4} (equivalent to a 3 MPa stress drop in rock mass with $\mu = 30$ GPa) for a MW2.5 event, a corner frequency of 8 Hz can be expected. With a P-wave velocity of

6,000 m/s and wanting to be five times the wavelength away would correspond to a wavelength of 750 m, meaning that sensors should ideally be at least 3 km away from the source to accurately capture this frequency. In this specific case, the most distant in-mine operational geophone was located 1.2 km away, indicating that even if it were a 1 Hz sensor it would not be far enough away to be sufficiently in the far field.
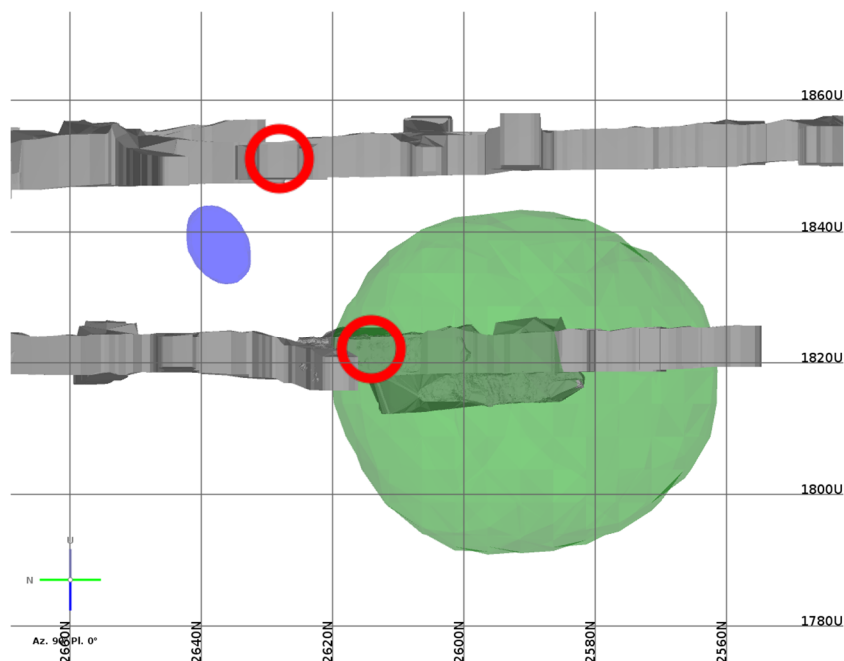

Figure 6 Section view showing the 95% location uncertainty regions of phase 1 (blue) and phase 3 (green). Red circles indicate approximate areas where damage was observed. The centres of the two regions are approximately 50 m apart
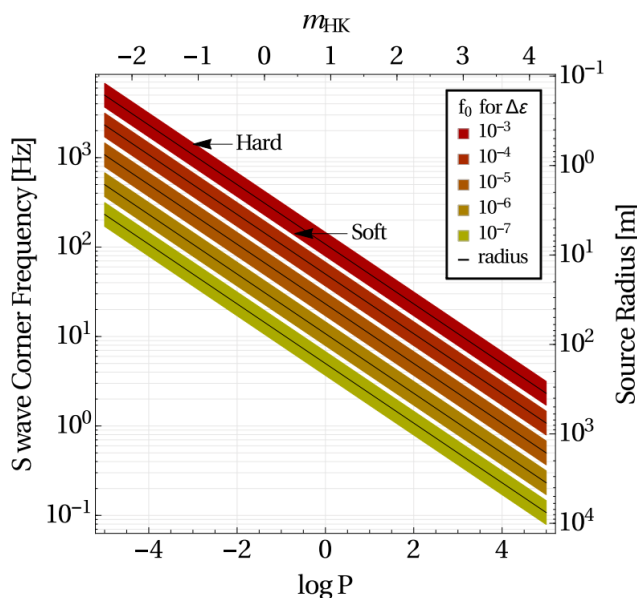

Figure 7 Expected corner frequency against moment magnitude (MHK, the same as MW) for different strain changes (Mendecki 2016)

To improve the estimation of the source parameters, waveforms from the local regional seismic network (RSN) (Wesseloo et al. 2011) were analysed. The RSN consists of several 4.5 Hz geophones situated around the Abitibi region. Figure 8 shows an example waveform of the event recorded at the most distant RSN station. The waveforms from these RSN sensors were analysed in conjunction with those from the in-mine network. Figure 9 compares the spectral fit using the in-mine geophones only with the combined in-mine

+ RSN set. The spectral fit using the in-mine sensors only appears reasonable but the low frequency plateau is not captured. When adding the RSN sensors the low frequency plateau is evident. Note that there is some overlap of frequencies covered by the two sensor sets, around 15–40 Hz, where the spectral levels of the two sets are consistent. When using the in-mine sensors only the event is estimated to have MW1.9, which increases to MW2.5 when the RSN sensors are incorporated. This can be compared to the National Resources Canada (NRCAN) estimate using the MN to MW conversions of Bent (2011) and Sonley & Atkinson (2005), respectively:

$$MW = MN0.93 - 0.22 \pm 0.19 \tag{1}$$

$$MW = MN1.03 - 0.61 \pm 0.1 \tag{2}$$

This estimates a NRCAN magnitude of MN2.8 as MW2.4 ± 0.19 or MW2.3 ± 0.1 (National Resources Canada 2024), in agreement with the MW2.5 found when using the RSN network.

Source parameters for the event, with and without the inclusion of the RSN network, are given in Table 3. It is important to note that due to limitations of the network, logP calculated using the in-mine and RSN networks is expected to be the most reliable parameter. When using the in-mine only sensors the low frequency plateau is not well captured, leading to an underestimation of seismic potency (or moment), and the corner frequency is not clear at all. Adding the RSN sensors helps capture the low frequency plateau and estimate seismic potency, however, the estimation of corner frequency is still somewhat uncertain. This is because the RSN sensors are notably further away than the in-mine sensors and the attenuation between the source and the RSN sensors is not known. The remote RSN sensors are also on the surface, which can introduce other local site effects (some surface sites show a resonance at around 20 Hz, likely related to sensor installation) and even, potentially, surface waves. Seven aftershocks were processed and were found to have static stress drops of around 0.5–1 MPa. The source parameters of these are expected to be more reliable and may indicate that the calculated corner frequency of the main event is slightly overestimated.

Table 3   Summary of estimated source parameters using the in-mine sensors only, and when adding the RSN sensors

Parameter	In-mine only	In-mine + RSN
logP	1.5	2.3
logE	7.2	7.3
chanf0 (Hz)	25	18
Static stress drop (MPa)	3.8	2.2

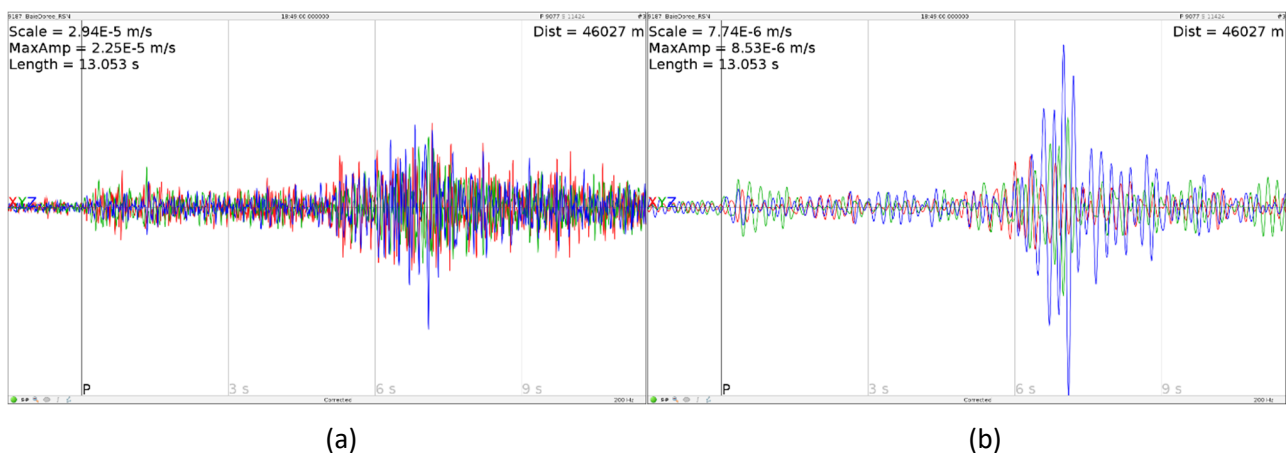(a)   (b)

Figure 8   Example waveform from the most distant operational sensor in the RSN that recorded the event, showing the raw waveforms on the left (a) and bandpass filtered waveforms between 1–6 Hz on the right (b)

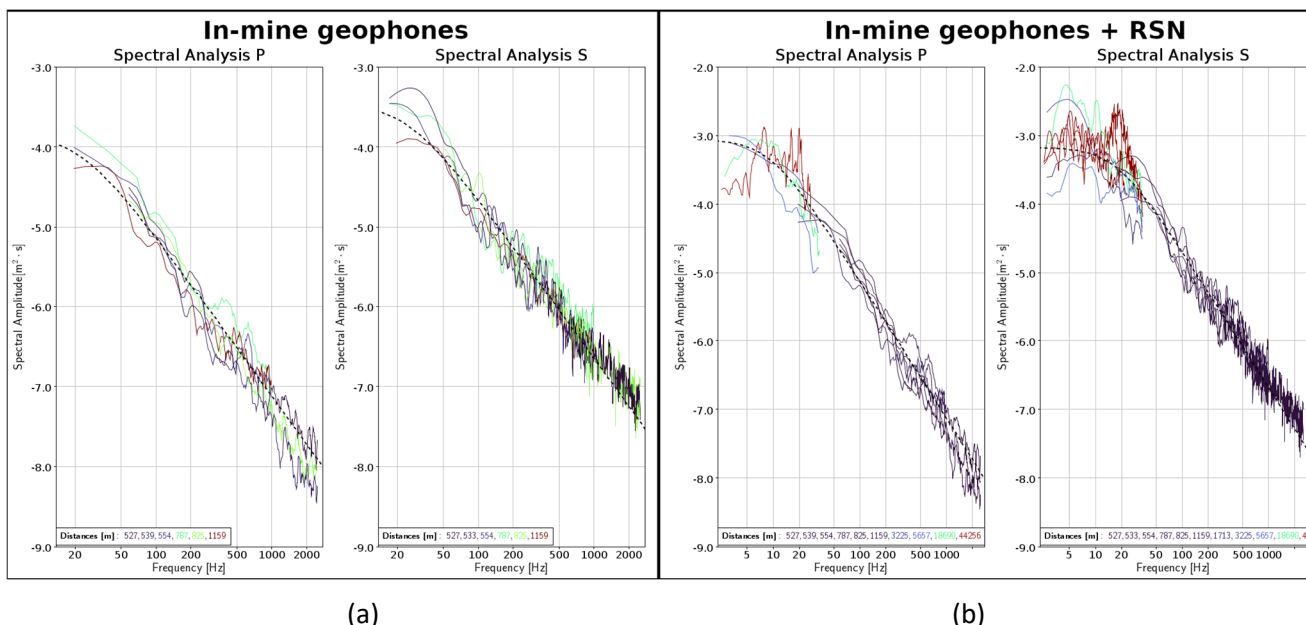(a)   (b)

Figure 9   Source spectra of the large event using the in-mine geophones only (a) and combining the in-mine sensors with those from the RSN (b). In both cases the data are coloured according to hypocentral distance

The next step after the source parameter estimation is to investigate the seismic source mechanism. It is immediately apparent that an in-mine network is not well suited to this task simply due to the size of the event, relatively small hypocentral distances and the frequency bandwidth of the sensors. Despite these limitations a point source moment tensor inversion was attempted. This was done utilising the full waveform methodology of Vavryčuk & Kühn (2012). The waveforms are bandpass filtered between 5 and 10 Hz and inversion is conducted in the displacement domain. Figure 10 shows the resultant waveform fit and source mechanism confidence plots (using a Monte Carlo method sampling for the mechanism type and orientation space).
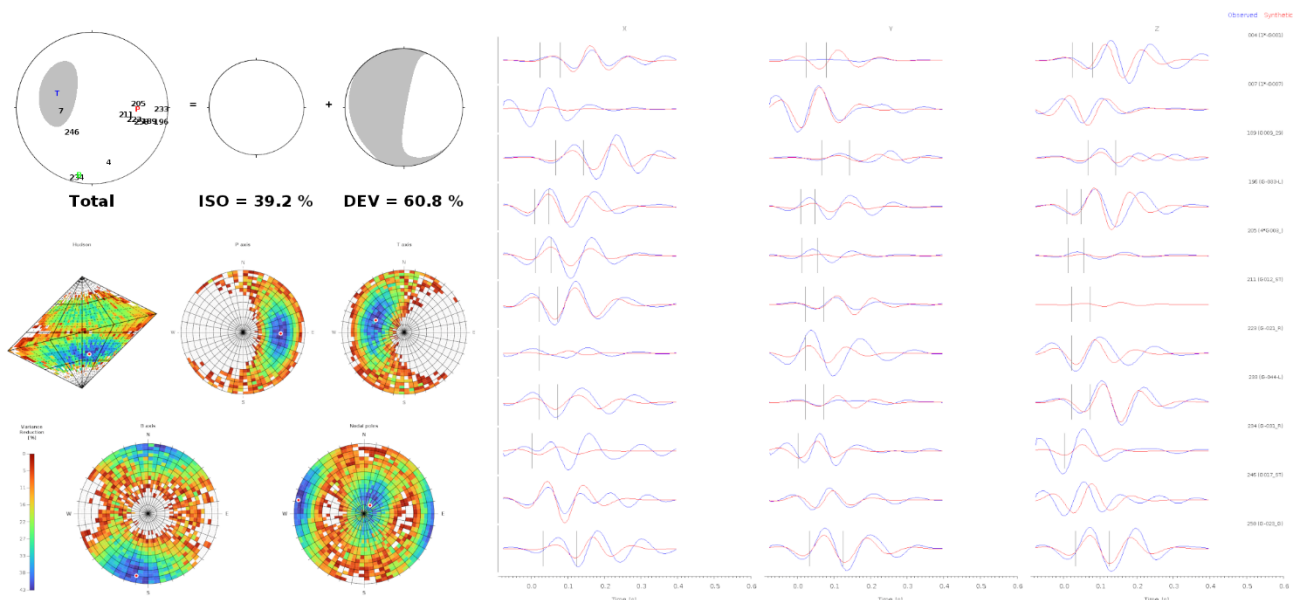

Figure 10   Source mechanism inversion plots. The resultant mechanism (top left) has a combined implosive and reverse faulting mechanism (lower hemisphere, beachball representation). The fit between the observed (blue) and modelled (red) waveforms is shown on the right. The lower-left plot shows the source mechanism confidence plots. Colour indicates the variance reduction (%)

The agreement between the observed (blue) and synthetic (red) waveforms in Figure 10 is fairly reasonable at most sites although a few discrepancies are visible (no polarities are reversed but there are some differences in amplitudes). Considering the magnitude of the event and the proximity of the sensors to the source, this result is not unexpected. The resultant source mechanism is a combination of slip (reverse faulting) and crush type, with the P-axis dipping to the east. The mechanism confidence plots indicate that the solution is reasonably constrained. The P-axis is quite well constrained in terms of dip, with similar fit found within ±10°, although the azimuth is less well constrained, up to around ±25°. The source type shows some scatter on the Hudson plot but remains in the lower portion of the diagram, indicating an implosive component.

4   Finite source analysis

The standard approach of conducting seismic source mechanism inversions treats the source as a point source, with all seismic waves originating from the same location. When it comes to very large seismic events in mines, the source can be tens or even hundreds of metres (e.g. Boskovic 2022), with different regions of the source radiating seismic waves at different times and clearly breaking the assumption of a point source. Furthermore, from a more practical perspective, large seismic events may cause damage to underground excavations at large distances from the initially processed event location. In some cases one may argue that this is due to location uncertainty, but there may be cases where a single seismic event causes multiple episodes of damage at different locations (examples such as Malovichko et al. 2018; Boskovic 2022; Cai & Kaiser 2018). This cannot be explained by location uncertainty nor simple ground motions from the source. In these situations the seismic source requires a more comprehensive description in terms of the spatial distribution of deformation, for both amount and type (shear or crush). Finite source inversion, a popular tool in crustal seismology, accomplishes this. Rather than assuming the deformation occurs at a single point, the seismic source is now described by a collection of subsources distributed in space, where the amount, type and orientation of deformation can vary for each subsource (to within reasonable limitations). Ide (2007) provides a good overview of finite source inversion theory in a crustal environment where the sources are constrained to slip-type events. However, in mining, this is not the case (Malovichko 2020; Malovichko & Rigby 2022) and seismic events may be due to slip- or crush-type sources (or a combination thereof). Malovichko et al. (2018) expanded the finite source methodology of Olson & Apsel (1982) so that it could also account for crush-type sources such as those that are frequently associated with mine excavation damage. In the finite source inversion each subsource is described by several variables: orientation of slip and/or convergence, amount of slip or convergence, location and origin time. As a typical finite source inversion will usually have tens, if not many more, subsources, the number of parameters involved in the inversion can quickly become extremely large. This large number of free variables can lead to cases where the inversion is able to perfectly replicate the recorded waveforms but the resultant source is not physically reasonable. It is therefore necessary to implement constraints on the finite source inversion so that the results can have a physically meaningful interpretation. This is done by prescribing the locations and types of sources, source initiation location and rupture propagation velocity. Various sources of geological, observational and seismic data may be used to help define these constraints. For example, the observed locations of strainburst damage can represent crush-type subsources, assuming that they happened as part of the main event. Structural models or the location and orientation of aftershocks can be used to define the primary slip plane and direction of slip in the case of slip-type events.

A few initial variants of the finite source inversion input source were tested. The final input finite source constructed is shown in Figure 11. The following aspects of data were used in the construction:

- Location and orientation of the slip plane were determined from point source inversion of the main event.

- The spatial extent of the source was based on aftershock distribution.

- Rupture velocity, the rate at which subsource origin time, t_0, propagates away from the initial hypocentre, was estimated at 800 m/s, based on waveform observations and the estimated location of different phase arrivals (Figure 6). This is in agreement with Chounet et al. (2018), who would have estimated 1,070 m/s for a stress drop of 2 MPa (considering the notable uncertainties).

- Crush-type subsource locations were determined based on underground observations.
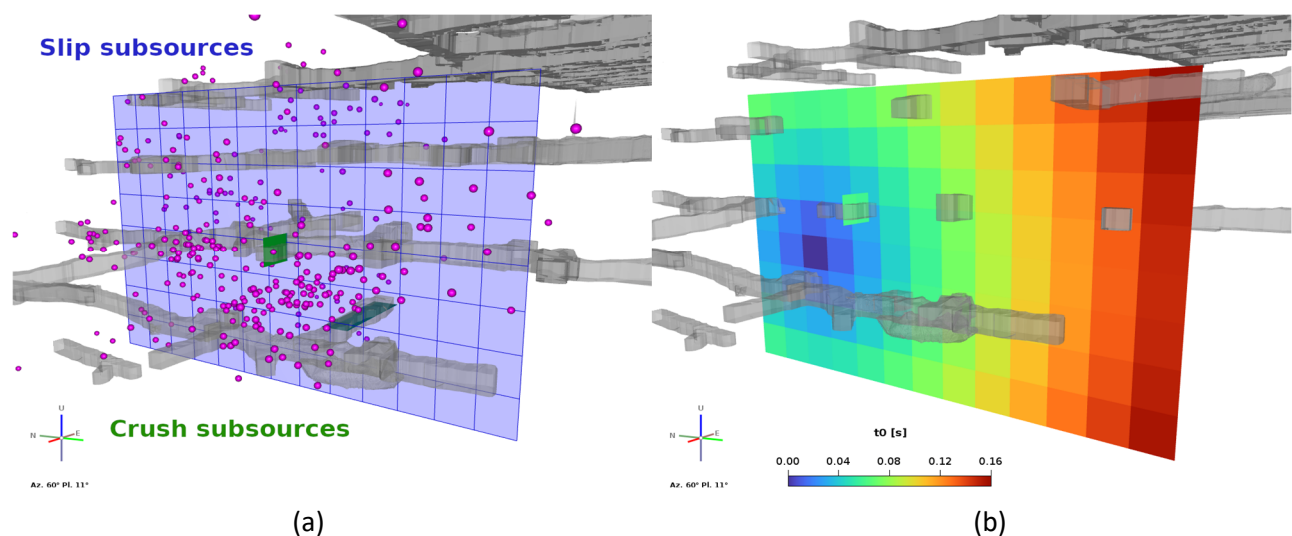

(a) (b)

Figure 11 Location of the input model slip (blue) and crush (green) subsources: (a) Locations of aftershocks (with MW > –2.0) recorded in the five hours following the event; (b) Distribution of t_0, the time at which subsources can 'turn on'

Figure 12 examines the evolution of the inverted seismic source slip and convergence distribution at different time steps. The source originates to the north, where traditional processing placed the location of the initial P-wave and S-wave arrivals, and propagates to the south. The finite source inversion also provides estimates of slip and convergence rates which can provide useful insight into understanding the dynamic load imposed on the ground support (Kaiser & Moss 2022). Figure 13 looks at the final distribution of these rates and the seismic potency of the subsources. The potency for each slip subsource is based on the area of the subsource multiplied by the slip, while for the crush subsources it is based on the convergence and ride.
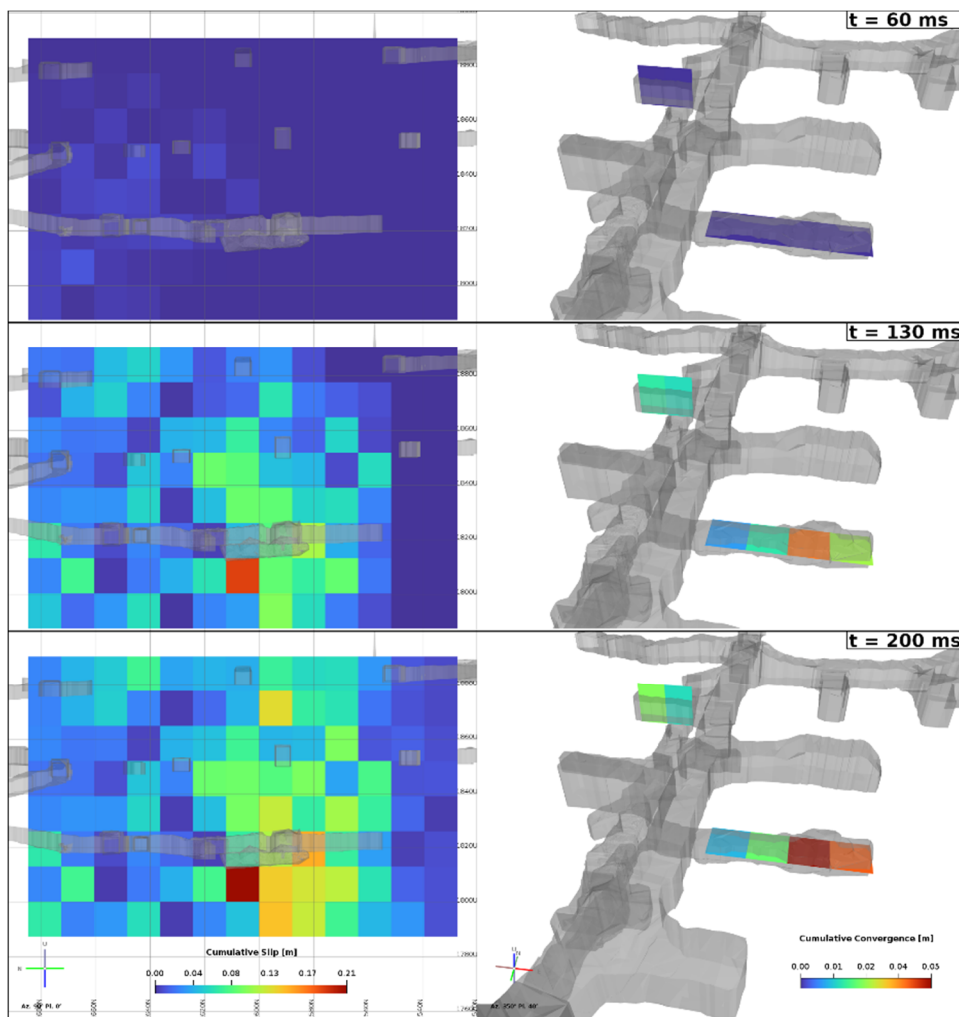
Figure 12 Evolution of the source over time, showing the cumulative slip at three different time intervals for the slip sources (left) and crush sources (right). The slip initiates to the north and propagates southward. Slip values remain fairly low for around the first 100 ms, at which time the deformation accelerates. The maximum slip found is around the centre part of the plane, deeper, and is estimated at 21 cm, although this is localised to a single subsource. A group of subsources around the centre–south have slip in the order of 10–15 cm. Almost all of the crush deformation occurred between t = 130 and 170 ms, and has a maximum of 5 cm of elastic convergence

The estimated slip velocities of the slip-type subsources can be compared to other methodologies such as McGarr (1991), which looks at the amplitude and frequency associated with high frequency pulses in the seismic waveforms. It is important to estimate these near-field ground motions to understand the dynamic load imparted on ground support in excavations close to the source. Table 4 lists the values inferred at a number of sensors and can be compared to the maximum slip rates from the finite source inversion in Figure 13. The two sets are seen to be in good agreement.

One of the utilities of constructing these finite source models is that it allows the expected ground motion from the source to be evaluated at any location of interest (e.g. where shakedown damage was observed, people experienced shaking or critical infrastructure is located). This is illustrated in Figure 14, where the observed waveforms are lowpass filtered below 100 Hz. The scatter plot shows good agreement between the observed and modelled peak ground velocity (PGV) values, with a root mean square error of log(PGV) = 0.278, which is considered quite low for ground motion prediction. The comparison is done on a per-component basis to account for the effects of the source mechanism and radiation patterns.

Table 4   Estimates of near source ground motion using the McGarr (1991) method for a select group of sensors

SiteID	R (m)	Peak acceleration (m/s²)	Peak slip velocity (m/s)
215	158	22.1	2.6
7	161	16.5	2.0
234	228	15.7	2.7
196	418	16.4	5.4
233	498	7.3	3.0
258	555	5.2	2.4
189	788	3.2	2.2
188	822	3.0	2.2

(a)   (b)
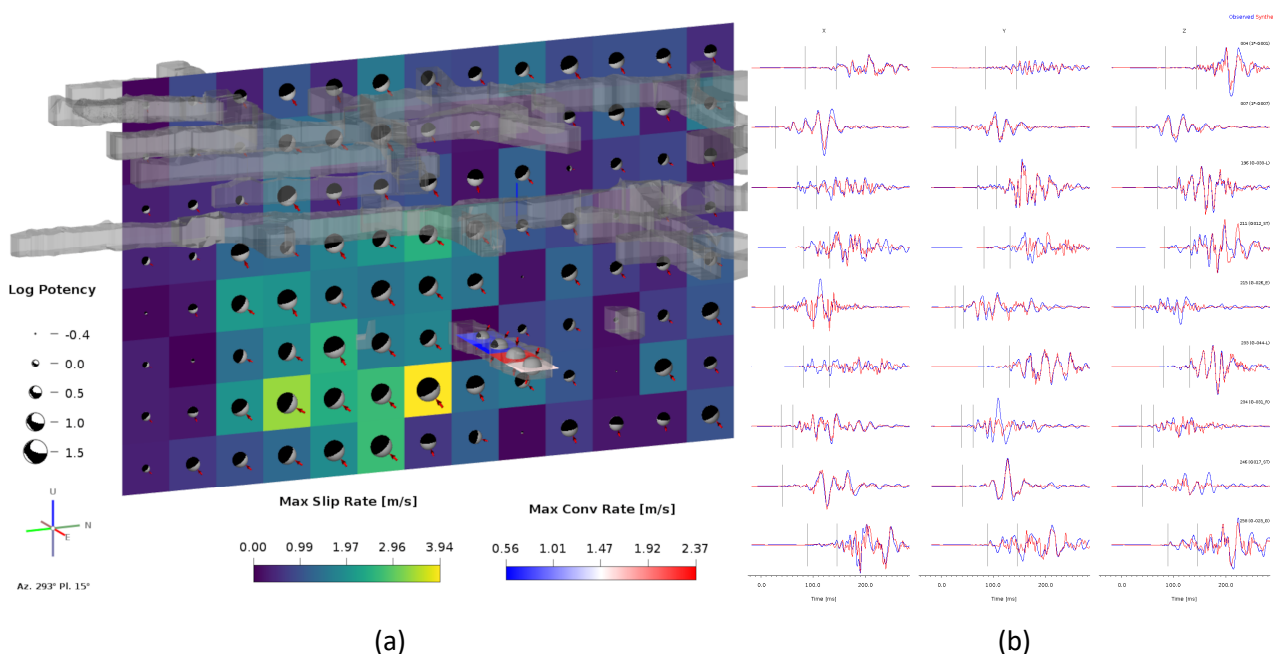
Figure 13   (a) View of the subsources showing the distribution of resultant maximum slip (vertical north–south plane, blue–yellow scale) and convergence (horizontal east–west plane, blue–red scale) rates. The highest slip rate was 3.94 m/s, localised to a single subsource, while the highest convergence rate was 2.37 m/s. A group of slip subsources in the centre had values around 1.5 to 2.5 m/s. Some crush subsources on the other side of the plane are not visible but had lower convergence rates (up to 1.1 m/s); (b) Comparison of observed (blue) and synthetic (red) waveforms for the final source
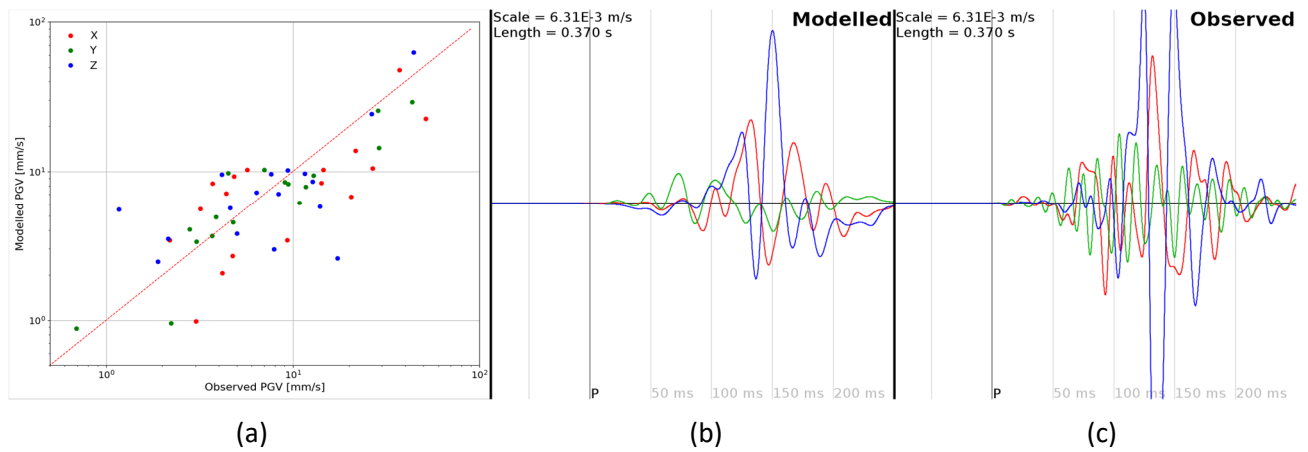
(a)   (b)   (c)

Figure 14   Scatter plot of the per-component observed and modelled peak ground velocities
(a) Comparison of the modelled (b) and observed (c) waveforms at one sensor with the same
time and amplitude scales. Time markers on the X-axes are measured relative to the P-wave
arrival. The modelled waveforms capture the emergent nature of the recorded seismograms and
have strong similarities (e.g. a strong S-wave with maximum amplitude on the Z component,
significant amplitude on the X component and low amplitude on the Y). The timing of the peaks
on different components are also very consistent (e.g. +X at t~130 ms, +Z at t~150 ms)

5   Understanding different source mechanisms

Another aspect of the data that can be investigated is understanding the different contributions from
slip-type and crush-type deformation to the overall seismic source. Two different approaches are used: firstly
the results from the finite source inversion are used by taking the final resultant subsources, splitting them
between crush-type and slip-type based on their source mechanism, and summing the totals to find the total
seismic potency (or moment) associated with each failure type. For the second approach a combination of
the source parameters of the event (when including the RSN) and underground observations is used.
Using the model described in Malovichko & Rigby (2022), the scalar seismic moment of crush-type sources
can be estimated from observed damage using Equation 3.

$$|M| \approx 2\frac{1-\nu}{1-2\nu}|\sigma_{max}|L_3\overline{L_A}\Delta d_f^A \tag{3}$$

Where ν is Poisson's ratio, σ_{max} is the maximum stress in the plane of the excavation, along the tunnel, $\overline{L_A}$
is the effective tunnel dimension and Δd_f^A is the increase in the depth of failure. It was assumed that ν = 0.21
(based on observed V$_P$/V$_S$ ratio) and a shear modulus of μ = 30 GPa. Bulking was observed in three locations,
which were assumed to be the different crush-type subsources. Table 5 summarises the effective moment
magnitude using Equation 3 for each location and in total. This total crush-type seismic moment (or potency,
P = 18.7 m³) is subtracted from the overall seismic moment (or potency, P = 210 m³, derived from source
parameters) to estimate slip contribution.

Table 5   Summary of seismic moment (and potency) and equivalent moment magnitude estimated from
observed bulking

Location	M (Nm)	P (m³)	logP	MW
1	3.6E+11	12.00	1.08	1.64
2	1.35E+11	4.50	0.65	1.36
3	6.48E+11	2.16	0.33	1.14
Sum	5.60E+11	18.66	1.27	1.77

Table 6 summarises the overall seismic moment for the different source types for the two approaches. It should be noted that these approaches can be considered independent. The finite source approach uses the cumulative potency from the inverted subsources based on in-mine sensors only. The other approach relies on the seismic moment from the RSN network and physical underground observations. Despite these two different approaches, the results in Table 6 are consistent: both confirming the hypothesis that the majority of deformation in the rock mass responsible for radiating seismic energy was due to shear motion rather than the sudden expansion of the depth of failure around excavations.

Table 6   Estimates of slip-type and crush-type contribution to the overall seismic moment

		P (m³)	logP	MW	% of total
Finite source inversion	Crush	45	1.65	2.02	6.05
	Slip	699	2.84	2.82	93.95
	Total	744	2.87	2.83	
Point source and observation	Crush	18.7	1.27	1.77	8.89
	Slip	191.3	2.8	2.44	91.11
	Total	210	2.32	2.47	

6   Interpretation of the source

The analysis of the seismic data presented above shows that the seismic source was complex and distributed in space. The seismic source mechanism and finite source inversion analysis indicate that the source was predominantly associated with shear deformation. This likely caused localised loading at some excavations, resulting in bulking in the walls parallel to the schistosity. While the source is seen to be mostly shear, there was no clear evidence of slip on a known geological feature. Rather it is interpreted as a shear dislocation of the 'pillar' between the vertically offset 317 and 320 levels, as illustrated in Figure 15.
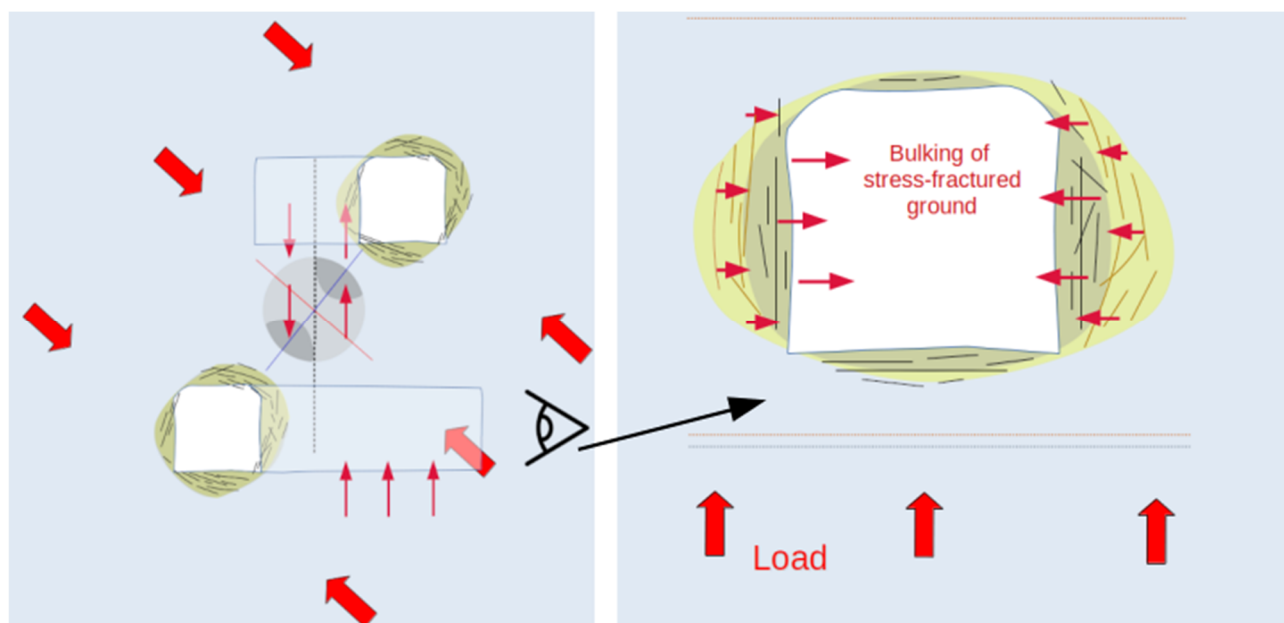

Figure 15   Schematic representation of the proposed seismic source mechanism, illustrating the shear dislocation of the 'pillar' between the vertically offset 317 and 320 levels on the left. On the right is a schematic representation of the seismic event-induced ground deformation which likely caused localised dynamic loading at some excavations, leading to bulking and displacement of fractured ground

7   Conclusion

Large seismic events in mines generate complex and difficult to process waveforms. However, tools are available to utilise these events as a source of rich and deep information that provides insight into the rock mass behaviour. To achieve this though, one must adopt the view that a seismic event represents more than just a dot in space with some associated parameters. It truly is a region of rock mass that experiences some spatio-temporal evolution of deformatio which leaves a record in the seismic observations. The analyses presented in this study illustrate the steps taken from first initial inspection and processing of the waveforms all the way through to using seismic data from different sources, the near field and far field, and underground observations to present a more comprehensive picture of what happened. It should be stated that the provided finite source inversion results are not considered as being a 100% accurate representation of reality but they do present a plausible explanation of what happened from a rock mechanics' perspective that is backed up by, and in agreement with, seismic evidence. This resultant finite source can then be used to gain a more accurate understanding of the dynamic load imparted on excavations, be it due to shaking from shear deformation or convergence rate from strainbursts.

The seismological analysis presented in the previous sections provides additional insights into the seismic response of mine excavations at great depth. The approach described here is new at LaRonde and should be further tested in the future. As more events are analysed in this manner, confidence in the approach can be gained. The seismic analyses, whether more traditional or advanced, must be combined with observations, damage mapping, deformation monitoring and other analysis tools, such as numerical modelling, to continue to improve seismic risk management practices at the mine.

Acknowledgement

References

Bent, AL 2011, 'Moment magnitude (MW) conversion relations for use in hazard assessment in eastern Canada', *Seismological Research Letters*, vol. 82, no. 6, pp. 984–990, https://doi.org/10.1785/gssrl.82.6.984

Boore, DM 1986, 'The effect of finite bandwidth on seismic scaling relationships', *Earthquake Source Mechanics*, American Geophysical Union.

Boskovic, M 2022, 'Challenges of resuming the production after a major seismic event at LKAB's Kiirunavaara mine', in MS Diederichs (ed.), *Proceedings of the 10th International Conference on Rockbursts and Seismicity in Mines*, Society for Mining, Metallurgy & Exploration, Englewood.

Cai, M & Kaiser, PK 2018, *Rockburst Support Reference Book*, vol. 1, MIRARCO Mining Innovation, Sudbury.

Chounet, A, Vallée, M, Causse, M & Courboulex, F 2018, 'Global catalog of earthquake rupture velocities shows anticorrelation between stress drop and rupture velocity', *Tectonophysics*, vol. 733, pp. 148–158, https://doi.org/10.1016/j.tecto.2017.11.005

Corthesy, R 2006, *Détermination des Contraintes in situ aux Niveaux Inférieurs des Mines Agnico-Eagle*, draft report, Division Mine LaRonde.

DGI Geoscience Inc. 2017, *LaRonde – Stress Inversion Study and Acoustic Televiewer Surveys (Technical Report L–434)*.

Gibowicz, SJ & Kijko, A 1994, 'Chapter 11: seismic spectra and source parameters', *An Introduction to Mining Seismology*, Academic Press, New York, https://doi.org/10.1017/CBO9781107415324.004

Goulet, A, Grenon, M, Woodward, K, Wesseloo, J & Morissette, P 2018a, 'Development of an integrated geotechnical database and associated analysis tools for excavation design in seismically active underground mines', *Proceedings of the 52nd U.S. Rock Mechanics/Geomechanics Symposium*.

Goulet, A, Grenon, M, Morissette, P, Woodward, K & Wesseloo, J 2018b, 'Properties of large-scale geological features and seismic responses affecting strainburst potential in deep underground mines', *Proceedings of the 10th Asian Rock Mechanics Symposium*.

Hanks, TC & Kanamori, H 1979, 'A moment magnitude scale', *Journal of Geophysical Research: Solid Earth*, vol. 84, no. B5, pp. 2348–2350, https://doi.org/10.1029/JB084iB05p02348

Hoek, E 1994, 'Strength of rock and rock masses', *International Society for Rock Mechanics News Journal*, vol. 2, no. 2, pp. 4–16

Ide, S 2007, 'Slip inversion', in G Schubert (ed.), *Treatise on Geophysics, Volume 4: Earthquake Seismology*, pp. 193–223.

Kaiser, PK & Moss, A 2022, 'Deformation-based support design for highly stressed ground with a focus on rockburst damage mitigation', *Journal of Rock Mechanics and Geotechnical Engineering*, vol. 14, no. 1, pp. 50–66, https://doi.org/10.1016/j.jrmge.2021.05.007

Karampinos, E, Hadjigeorgiou, J, Hazzard, J & Turcotte, P 2015, 'Discrete element modelling of the buckling phenomenon in deep hard rock mines', *International Journal of Rock Mechanics and Mining Sciences*, vol. 80, pp. 346–356, https://doi.org/10.1016/j.ijrmms.2015.10.007

Malovichko, D 2020, 'Description of seismic sources in underground mines: theory', *Bulletin of the Seismological Society of America*, vol. 110, no. 5, pp. 2124–2137, https://doi.org/10.1785/0120200093

Malovichko, D, Cuello, D & Rojas, E 2018, 'Analysis of damaging seismic event on 24 December 2011 in the Pilar Norte sector of El Teniente mine', in Y Potvin & J Jakubec (eds), *Caving 2018: Proceedings of the Fourth International Symposium on Block and Sublevel Caving*, Australian Centre for Geomechanics, Perth, pp. 637–650, https://doi.org/10.36487/ACG_rep/1815_49_Malovichko

Malovichko, D & Rigby, A 2022, 'Description of seismic sources in underground mines: dynamic stress fracturing around tunnels and strainbursting', *ARxiv*, https://doi.org/10.48550/arXiv.2205.07379

McGarr, A 1991, 'Observations constraining near-source ground motion estimated from locally recorded seismograms', *Journal of Geophysical Research: Solid Earth*, vol. 96, no. 91.

Mendecki, AJ 2016, *Mine Seismology Reference Book: Seismic Hazard*, Institute of Mine Seismology, Kingston, https://www.imseismology.org/publications/

Monecke, T, Mercier-Langevin, P, Dubé, B & Frieman, BM 2017, *Geology of the Abitibi greenstone belt*, in T Monecke, P Mercier-Langevin, & B Dubé (eds.), A*rchean Base and Precious Metal Deposits, Southern Abitibi Greenstone Belt, Canada*, vol. 19, https://doi.org/10.5382/Rev.19.01

National Resources Canada 2024, *Search the Earthquake Database,* viewed 17 May 2024, https://www.earthquakescanada.nrcan.gc.ca

Nordström, E, Dineva, S & Nordlund, E 2017, 'Source parameters of seismic events potentially associated with damage in block 33/34 of the Kiirunavaara mine (Sweden)', *Acta Geophysica*, vol. 65, no. 6, pp. 1229–1242, https://doi.org/10.1007/s11600-017-0066-1

Olson, A & Apsel, R 1982, 'Finite faults and inverse theory with applications to the 1979 Imperial Valley earthquake', *Bulletin of the Seismological Society of America*, vol. 72, pp. 1969–2001.

Ouellet, A, Seguineau de Preval, C & Andrieux, P 2024, *LaRonde Mine – Numerical Modelling and Risk Analysis (Technical Report 2253-LAR-007-R-20240409-F)* A2GC, Montréal

Sasseville, G, Turcotte, P & Falmagne, V 2022, 'Control measures to manage seismic risk at the LaRonde mine, a deep and seismically active operation', *Proceedings of the 56th U.S. Rock Mechanics/Geomechanics Symposium*, https://doi.org/10.56952/ARMA-2022-0625

Sonley, E & Atkinson, GM 2005, 'Empirical relationship between moment magnitude and Nuttli magnitude for small-magnitude earthquakes in southeastern Canada', *Seismological Research Letters*, vol. 76, no. 6, pp. 752–755, https://doi.org/10.1785/gssrl.76.6.752

Vavryčuk, V & Kühn, D 2012, 'Moment tensor inversion of waveforms: a two-step time-frequency approach', *Geophysical Journal International*, vol. 190, no. 3, pp. 1761–1776, https://doi.org/10.1111/j.1365-246X.2012.05592.x

Wesseloo, J, Hudyma, MR & Harris, P 2011, 'A community based seismic system for obtaining regional and local seismic data of strategic importance', in Y Potvin (ed.), *Strategic versus Tactical 2011: Proceedings of the Fourth International Seminar on Strategic versus Tactical Approaches in Mining*, Australian Centre for Geomechanics, Perth, pp. 159–168, https://doi.org/10.36487/ACG_rep/1108_12_Wesseloo